

Electric Field-Assisted Sintering of Gadolinium-Doped Ceria: Sintering and Grain Growth Kinetics

S. K. Sistla^{*1}, T. Mishra², Y. Deng¹, A. Kaletsch¹, M. Bram², C. Broeckmann¹

¹Institute for Materials Applications in Mechanical Engineering, RWTH Aachen University, Augustinerbach 4, D-52062 Aachen, Germany

²Institute of Energy and Climate Research IEK-1: Materials Synthesis and Processing, Forschungszentrum Jülich GmbH, D-52425 Jülich, Germany

received June 18, 2019; received in revised form August 17, 2019; accepted October 18, 2019

Abstract

The densification and grain growth kinetics during field-assisted sintering of gadolinium-doped (10 mol%) ceria (GDC10) were analyzed by conducting isothermal sintering experiments. The model parameters, namely, a stress exponent of ~ 2 and apparent activation energy of ~ 260 kJ/mol for the densification have been determined experimentally. Subsequently, the grain growth has been described by a power law with an exponent of 2 and an activation energy of ~ 200 kJ/mol. Such values suggest that the dominating densification mechanism combines both diffusion and dislocation motion. A numerical model has been utilized to predict the densification curves, which show a satisfactory fit with the experimental curves. Particularly, it has been shown that grain growth kinetics, explicitly, needs to be taken into account in the densification models, to accurately predict the shrinkage during sintering.

Keywords: Field-assisted sintering technology (FAST), gadolinium-doped ceria, modeling, densification, grain growth

I. Introduction

Field-assisted sintering technology (FAST), also known as Spark Plasma Sintering (SPS), is defined as a low-voltage, direct current (DC) pulsed-activated pressure-assisted sintering and synthesis technique¹. It facilitates the manufacturing of dense materials at lower temperatures and with shorter sintering cycle times than conventional free sintering and hot-pressing sintering techniques. Enhanced densification and inhibited microstructure evolution have been observed with the FAST/SPS technique owing to the combination of applied uniaxial pressure, direct heat transfer, shorter dwell times and high heating rates².

CeO₂ is one of the most established materials for investigating the effect of mixed ionic and electronic conduction (MIEC), due to its high electrical conductivity at high temperatures and its resistance to harsh environmental conditions³. Rare earth elements are preferentially used for A-site doping since their atomic radii fit quite well to the ceria lattice parameters. Furthermore, gadolinium-doped ceria (GDC) is used as electrolyte material for intermediate temperature solid oxide fuel cells (IT-SOFCs)⁴ and is applied as a diffusion barrier layer in metal-supported fuel cells to avoid inter-diffusion between metallic substrate and anode as well as between electrolyte and cathode^{5,6}.

To understand the densification mechanisms during FAST/SPS, different techniques have been used as described in the relevant literature. Owing to the restriction

of radial displacement $\epsilon_{xx} = \epsilon_{zz} = 0$ in the graphite dies, the ratio between densification and uniaxial strain rates is fixed and their relation is described in Eq. (1).

$$\dot{\epsilon}_{yy} = \frac{\dot{\rho}}{\rho} \quad (1)$$

where $\dot{\epsilon}_{yy}$ is the strain rate in the direction of applied load, $\dot{\rho}$ is the densification rate and ρ the instantaneous relative density. Assuming that creep is the dominating densification mechanism enables the application of standard creep equations for evaluating the densification kinetics^{7–12}. The primary aim of this study is to determine the creep and grain growth parameters based on comprehensive analysis of isothermal sintering FAST/SPS experiments at temperatures ranging between 800 °C and 1400 °C, dwell times ranging from 0 to 6 minutes with a constant heating rate of 100 K/min and a constant uniaxial compaction pressure of 50 MPa.

II. Experimental Methods

(1) Characterization of the raw powder

The commercially available gadolinium-doped (10 mol%) ceria (GDC10) powder (Fuel Cell Materials), which had a specific surface area of 10.572 m²/g and a mean particle size of ~ 80 nm, was selected as the starting material. Scanning Electron Microscopic (SEM) and Transmission Electron Microscopic (TEM) images of the as-received powder are shown in Fig. 1.

* Corresponding author: s.sistla@iwm.rwth-aachen.de

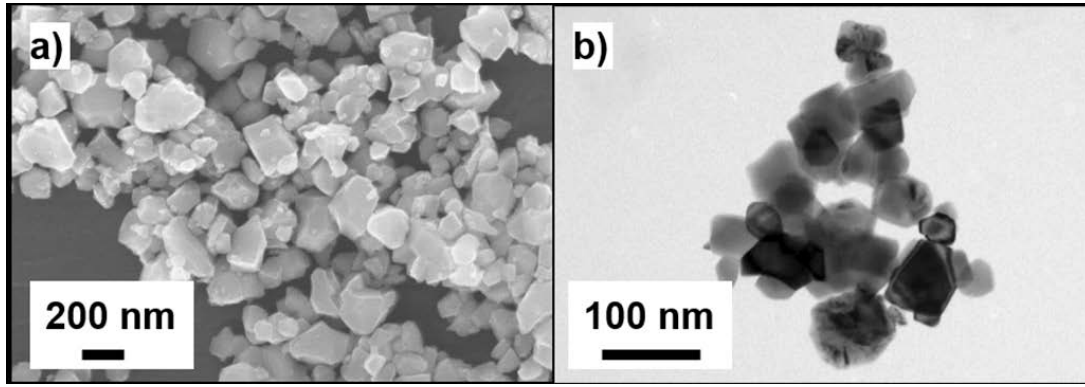


Fig. 1: GDC10 Powder under a) Scanning Electron Microscope b) Transmission Electron Microscope.

(2) FAST experiments

All FAST/SPS experiments were conducted on the as-received GDC10 powder in vacuum using FCT HP D 25–2 (FCT Systeme, Germany). The FAST/SPS graphite die (graphite type R7710, SGL Carbon GmbH, Germany) with a wall thickness of 10 mm and an internal diameter of 20 mm was filled with 6 g powder between two graphite punches. To facilitate better contact prior to the FAST/SPS process and for easy removal of punches post the FAST/SPS experiments, a graphite foil of 0.4 mm thickness was used between the punches and the die and between the powder and the punches. The assembled graphite tool set-up was pre-compacted at room temperature with a uniaxial pressure of 16 MPa, which corresponds to the minimum pressure applied in the FAST/SPS equipment. The initial sample height was around 5 mm, which led to an initial relative density of around 50 %. A constant pressure of 50 MPa was applied before the heating cycle and was released shortly after surpassing the defined dwell time. For the identification of densification parameters, FAST/SPS experiments were performed at temperatures between 800–1200 °C with a constant dwell time of 6 minutes. On the other hand, to identify the parameters of the grain growth law, isothermal FAST/SPS experiments were performed at temperatures between 1000–1400 °C and with different dwell periods (0, 2, 4, 6 min). Furthermore, a constant heating rate of 100 K/min was also adopted in the experiments. The thermal expansion of the tools and the machine was considered by conducting correction experiments with dense GDC10 samples and subtracting the measured axial movement of the punch from the original sintering experiments. The end densities of the sintered samples were then measured using the Archimedes method.

(3) Microstructural analysis

The sintered samples were embedded in an epoxy material, finely polished, demolded and then thermally etched at temperatures of approximately 100 K lower than the corresponding sintering temperatures for 15 minutes. Microstructural images were taken of the sample with a high-resolution scanning electron microscope (LEO 982, Zeiss, Germany). The image analysis program Lince (TU Darmstadt, Germany) was used to determine the average grain size by means of the linear intercept method. To achieve a good statistical estimation of the grain size, images were

taken at three different locations. On average, at least 300 grains were measured and an average grain size with a standard deviation was determined.

III. Macroscopic sintering behavior

(1) Densification kinetics

Since standard creep equations can be utilized to understand the densification mechanisms in FAST, the approach utilized by Bernard-Granger^{7,8} has been applied here, whereby the macroscopic strain rate is defined in Eq. (2)

$$\dot{\epsilon}_{yy} = \frac{\dot{\rho}}{\rho} = \frac{B\Phi\mu_{\text{eff}}b}{kT} \left(\frac{b}{G}\right)^p \left(\frac{\sigma_{\text{eff}}}{\mu_{\text{eff}}}\right)^n \quad (2)$$

where, $\dot{\epsilon}_{yy}$ is the strain rate in the axial direction, B is a constant, Φ is the diffusion coefficient, μ_{eff} the instantaneous shear modulus, b the Burgers vector, k the Boltzmann's constant, T the temperature, G the grain size, p the grain size exponent, σ_{eff} the instantaneous effective stress acting on the powder and n is the stress exponent. The instantaneous relative density is calculated with the expression in Eq. (3),

$$\rho = \rho_f \frac{L_f}{L} \quad (3)$$

where ρ_f is the final relative density determined as the ratio between the final density calculated with the Archimedes method and the theoretical density of GDC10 (7.128 g/cm³), L_f the final height and the L the instantaneous height. In the plots in the following sections, the relative density is plotted as a percentage value. The diffusion coefficient is described by an Arrhenius equation as in Eq. (4),

$$\Phi = \Phi_0 \exp\left(-\frac{Q_d}{RT}\right) \quad (4)$$

where Φ_0 is the pre-exponential term, Q_d the activation energy of the densification mechanism and R the gas constant. Since the applied macroscopic stress, σ_{ex} , is magnified at the microscopic level, it implies that the stress term in the creep equation has to be replaced with an effective stress term, σ_{eff} , which is dependent on the instantaneous relative density of the powder compact. Thereby, the effective stress and the effective shear modulus are defined as in Eqs. (5) and (6)^{7,8}

$$\sigma_{\text{eff}} = \frac{1 - \rho_0}{\rho^2(\rho - \rho_0)} \sigma_{\text{ex}} \quad (5)$$

$$\mu_{\text{eff}} = \frac{E_{\text{th}}}{2(1 + \nu_{\text{th}})} \frac{(\rho - \rho_0)}{(1 - \rho_0)} \quad (6)$$

where ρ_0 is the initial relative density, ρ the instantaneous relative density and E_{th} is Young's modulus and ν_{th} the effective Poisson's ratio. Mogensen *et al.*³ reported values of 165 GPa and 0.3 for Young's modulus and Poisson's ratio, respectively, for dense pure ceria at room temperature, and these values have been adopted in this study. Generally, these values decrease with increasing temperatures, however, here these values were considered independent of temperature^{7, 8, 13, 14}.

(2) Grain growth kinetics

Generally, the grain size evolution during sintering is dependent on temperature and sintering time. The grain growth kinetics are, generally, determined from isothermal sintering experiments. In the present work, a grain growth law for polycrystalline materials, from Ni *et al.*¹⁵, has been chosen and is defined as in Eq. (7).

$$G_t^p - G_0^p = Kt = K_0 t \exp\left(-\frac{Q_g}{RT}\right) \quad (7)$$

where G_t is the average grain size at time t , G_0 is the initial grain size, p is the grain growth exponent typically between 2–4 and may also depend on temperature, K is a rate constant, K_0 is a pre-exponential constant and Q_g is the apparent activation energy for grain growth. Here, as used in the works of Ni *et al.*¹⁵, the value of 2 has been used for the grain growth exponent p and independent of temperature.

IV. Results

(1) Sintering analysis with microstructure characterization

Fig. 2 presents the evolutions of the relative density and densification rate as functions of temperature for the FAST/SPS experiment conducted at a sintering temperature of 1400 °C, holding time of 6 min and uniaxial pressure of 50 MPa. The sample had an initial density of around 50 % and the maximum density of around 94 % has been obtained with sintering at 1400 °C. It was also observed that the densification of the GDC10 powder compact begins at temperatures of around 800 °C, and at around 1075 °C achieves a peak densification rate that

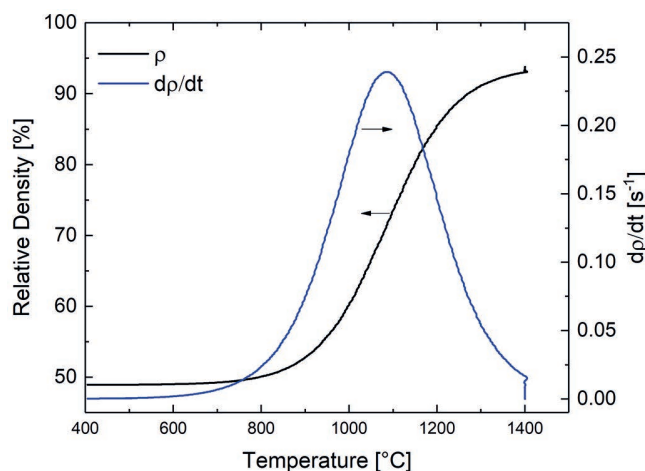


Fig. 2: Relative density and densification rate as a function of temperature for GDC10 sintered at 1400 °C with 100 K/min and constant pressure of 50 MPa.

subsequently decreases with increasing temperature to 1400 °C. Thus, the focus of this study has been the investigation of densification and grain growth in the temperature regime between 800 and 1400 °C.

Fig. 3 shows the relative densities determined with the Archimedes' method at sintering temperatures between 800 and 1400 °C and dwell times between 0 and 6 minutes. At 800 °C, the relative density changed from the initial relative density of 50 % to around 60 %, which is induced by the change in uniaxial pressure from 16 MPa to 50 MPa. It can be observed that the relative density change is independent of the dwell times at 800 °C, which is the lowest sintering temperature. It is also apparent that the relative density increases with increasing sintering temperatures and reaches a saturated value of around 94 % at a sintering temperature of 1200 °C and dwell time of 6 minutes. Any further increase in sintering temperature and holding time provides no significant change in the relative density. Higher sintering temperatures and dwell time only induce grain growth. This can be observed in the microstructure images (in Fig. 4) of GDC10 samples sintered at 1400 °C. Furthermore, it can be seen that the grain size also increases for progressing dwell times.

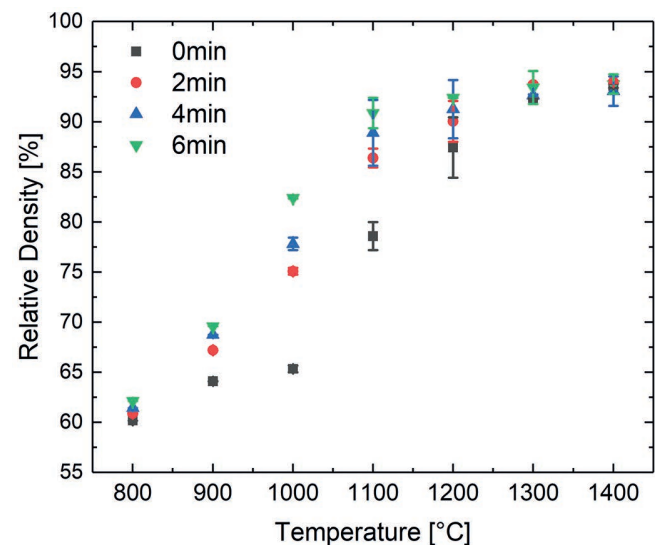


Fig. 3: Relative density as a function of temperature obtained for sintering temperatures of 800–1400 °C and dwell times of 0 to 6 min.

Fig. 5 shows the sintering trajectory of GDC10, where in the evolution of grain size of the sintered GDC10 samples with different sintering temperatures and dwell times are presented. The number on top of each colored block represents the dwell time, and the color of the block corresponds to the sintering temperature. Below the sintering temperature of 1200 °C and dwell time of 2 minutes, negligible grain growth is observed with grain size values ranging between 0.1 μm and 0.2 μm, which can be approximated to the initial grain size of the GDC10 powder particles. At sintering temperature of 1200 °C and dwell time of 4 minutes, there is a transition in the microstructure with an exponentially increased grain size to high temperatures and longer dwell times.

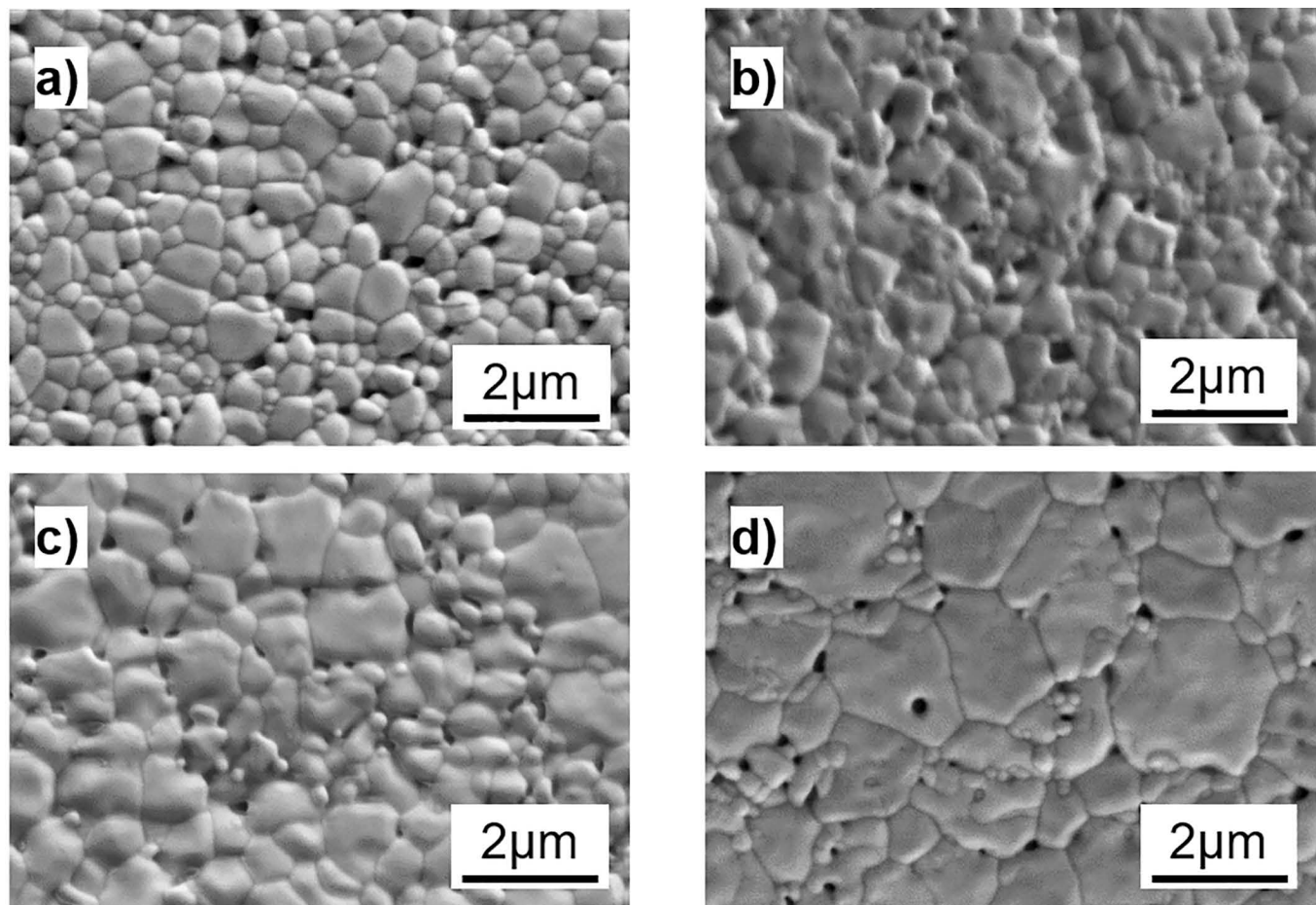


Fig. 4: Microstructure of GDC10 samples sintered at 1400 °C and different holding times a) 0 min, b) 2 min, c) 4 min d) 6 min.

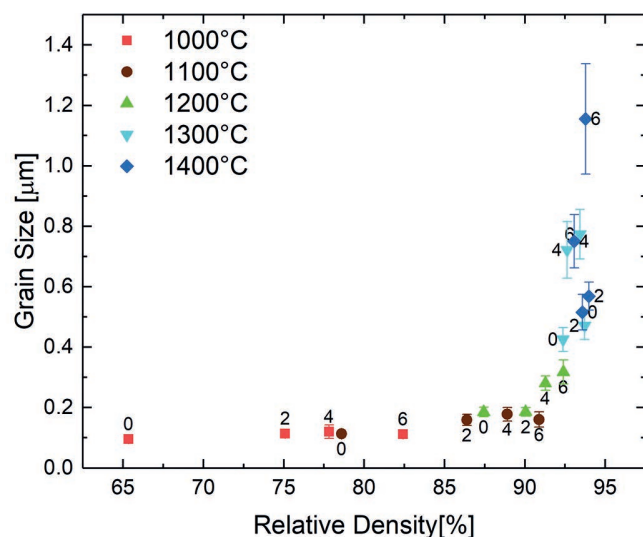


Fig. 5: Evolution of grain size plotted against relative density for different sintering temperatures (1000–1400 °C) and dwell times (0–6 min).

(2) Characterization of the densification behavior

Since the sintering temperature of 800 °C has no influence on the relative density and sintering temperatures higher than 1200 °C lead to grain growth, for the characterization of the densification behavior, temperatures between 900–1100 °C and the longest dwell time of 6 min-

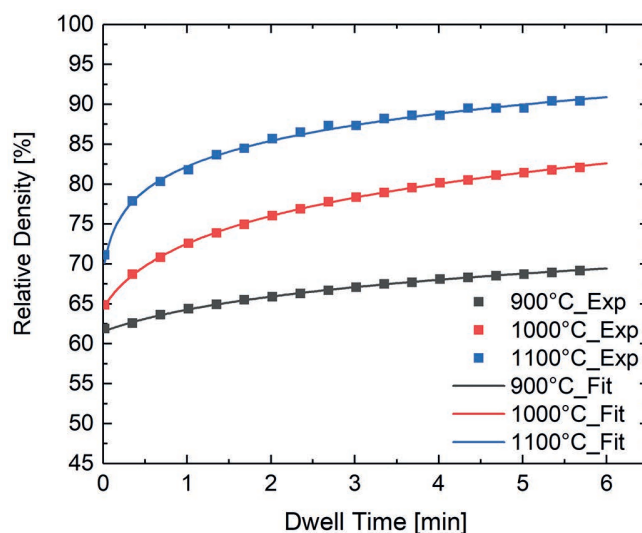


Fig. 6: Relative density obtained for different sintering temperatures as a function of dwell time according to Eq. (3).

utes have been utilized. Fig. 6 presents the different densification curves as a function of the dwell time. These values, at the different temperatures, have been calculated from Eq. (3). In order to determine the stress exponent n , Eq. (2) was rewritten as shown in Eq. (8). By keeping the temperature constant and assuming that there is negligible grain growth in the temperature range between 900

and 1100 °C, we can plot a double logarithmic plot with the left-hand side of Eq. (9) against the right-hand side, which leads to a linear curve, and the slope of this curve is the effective stress exponent n .

$$\frac{1}{\mu_{\text{eff}}} \cdot \frac{\dot{p}}{\rho} = K_0 \frac{\Phi}{T} \left(\frac{\sigma_{\text{eff}}}{\mu_{\text{eff}}} \right)^n \left(\frac{b}{G} \right)^p \quad (8)$$

$$\ln \left(\frac{1}{\mu_{\text{eff}}} \cdot \frac{\dot{p}}{\rho} \right) = n \ln \left(\frac{\sigma_{\text{eff}}}{\mu_{\text{eff}}} \right) + K_1 \quad (9)$$

Fig. 7 shows that the way the value of n is calculated for each sintering temperature. It can be observed that the R^2 values for each of the fits are larger than 0.99, which shows that the fitted lines fit the data better. For the temperature regimes between 900–1100 °C, an average value of 2.02 ± 0.16 is calculated.

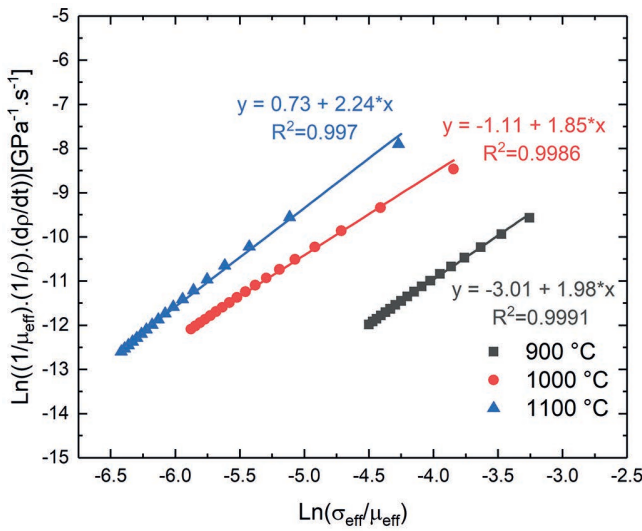


Fig. 7: Stress exponent calculated for sintering temperatures from 900–1100 °C and dwell time of 6 min.

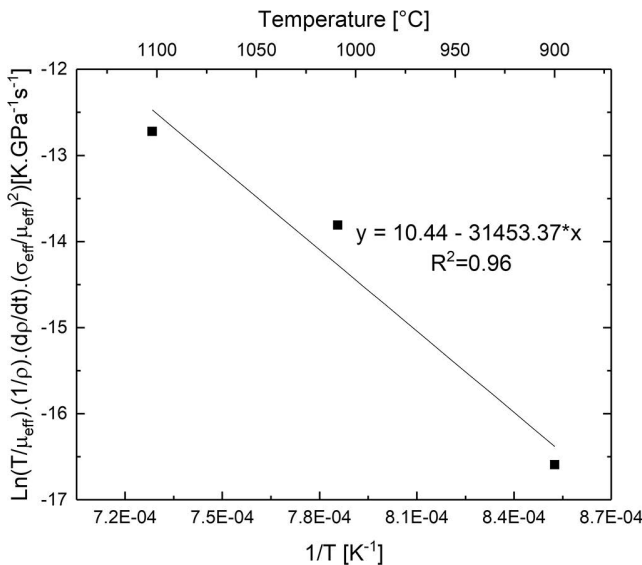


Fig. 8: Apparent activation energy for densification, Q_d , when $n \approx 2.02$ for the heating rate of 100 K/min and a uniaxial pressure of 50 MPa.

Subsequent to the calculation of the stress exponent, the activation energy is calculated at a constant value of the

densification rate (\dot{p}/ρ , here $1 \times 10^{-3} \text{ s}^{-1}$) and with an average stress exponent of 2. From Fig. 5, it appears that the grain size is constant at sintering temperatures of below 1200 °C and dwell time of 2 minutes. Making this assumption, we can rewrite Eq. (2) as shown in Eq. (10) to calculate the activation energy for densification Q_d . Finally, the left-hand side of Eq. (10) is plotted as a function of $1/T$ in an Arrhenius plot (Fig. 8). The slope of the line, with a high coefficient of determination (R^2) value, on multiplication with the gas constant ($R = 8.314 \text{ J/molK}$) leads to an average value of Q_d around 261.5 kJ/mol.

$$\ln \left(\frac{T}{\mu_{\text{eff}}} \left(\frac{\mu_{\text{eff}}}{\sigma_{\text{eff}}} \right)^n \frac{\dot{p}}{\rho} \right) = -\frac{Q_d}{RT} + K_2 \quad (10)$$

(3) Grain growth behavior

As seen in Fig. 5, the grain size is dependent on temperature and dwell time. For GDC the grain growth exponent assumed by Chen *et al.*¹⁶ and utilized in the works of Ni *et al.*¹⁵ is used. Here, as used in the works of Ni *et al.*¹⁵, the value of 2 has been used for the grain growth exponent p and independent of temperature. In order to determine the activation energy of grain growth, grain sizes from isothermal sintering experiments are determined and plotted in Fig. 9. As pointed out in Section IV.(1), no or negligible grain growth is observed at sintering temperatures below 1200 °C and dwell time of 2 minutes. This is again illustrated in Fig. 9.

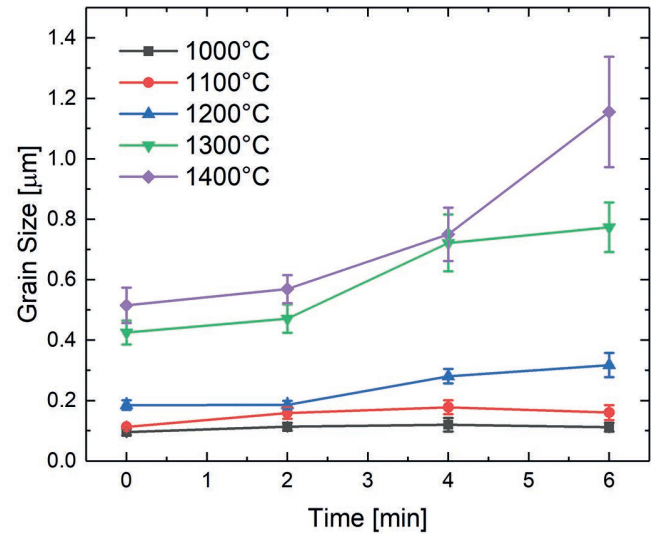


Fig. 9: Variations of average grain size versus isothermal time at different temperatures.

Eq. (7) is rewritten as Eq. (11). By means of plotting the left-hand side vs $1/T$ in an Arrhenius plot (Fig. 10), the average apparent activation energy of around 200 kJ/mol has been estimated as the slopes calculated for experiments with dwell time between 0 and 6 minutes. The Pearson's correlation coefficients for all the linear fitting in Fig. 10 are lower than -0.96, suggesting a strong linear correlation with the fit data.

$$\ln (G_t^2 - G_0^2) = \ln K_0 + \ln t - \frac{Q_g}{RT} \quad (11)$$

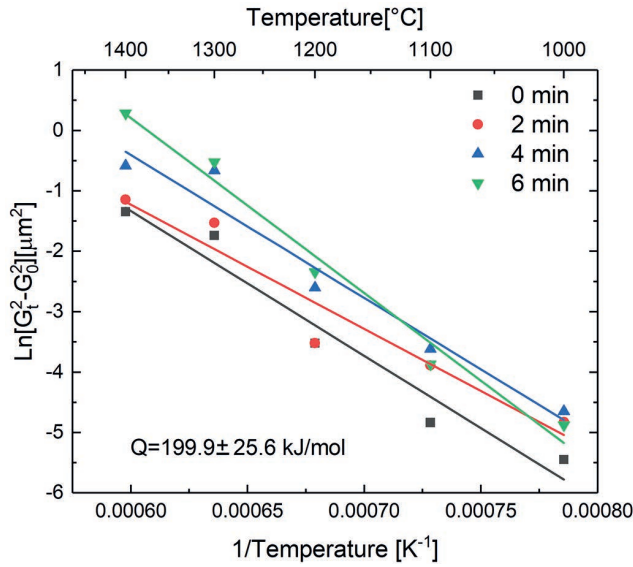


Fig. 10: Apparent activation energy for grain growth, when $p = 2$ for heating rate of 100 K/min and a uniaxial pressure of 50 MPa.

(4) Densification model

The densification model described in Eq. (2) with the additional equations has been implemented in MATLAB utilizing the parameters summarized in Table 1 and additional equations defined in Sections III (1) and III (2). For the modeling, an initial grain size of 80 nm has been utilized and the corresponding initial relative densities have been adopted. Fig. 11 indicates the experimental temperature profiles with a heating rate of 100 K/min from 500 °C, where the black, red and blue curves are the curves for sintering at 900, 1000 and 1100 °C, respectively. Additionally, the experimental evolution of the relative density for these temperatures is also presented as solid symbols (square for experiment sintered at 900 °C, circle at 1000 °C and triangle at 1100 °C). It should be noted that the initial density of the 900 °C experiment is around 58 %, of 1000 °C is around 55 % and of 1100 °C is around 50 %. Furthermore, the evolution of relative densities for these temperatures determined using the model are also presented as dash-dot lines. In the modeling of densification, the grain growth law, with the parameters determined in the previous section, have also been integrated. It is seen that the calculated relative densities, for all three sintering temperatures, are accurate in the isothermal regions when they are compared with the experimental evolutions.

Fig. 12 presents the experimental mean grain size as a function of temperature for the investigated temperatures

(900–1100 °C), depicted by the black solid squares and their corresponding standard deviations depicted by the error bars. Fig. 12 also presents the estimated homogeneous grain sizes (marked in red circles) for the corresponding temperatures. It is also seen that the estimated grain sizes lie well within the error regions of the experimental values, highlighting the effectiveness of the method used in this work. Since the activation energy is calculated from the linear regression analysis (Fig. 10), it can be presumed that the model can be used for analysis at the high-temperature regimes (1200–1400 °C).

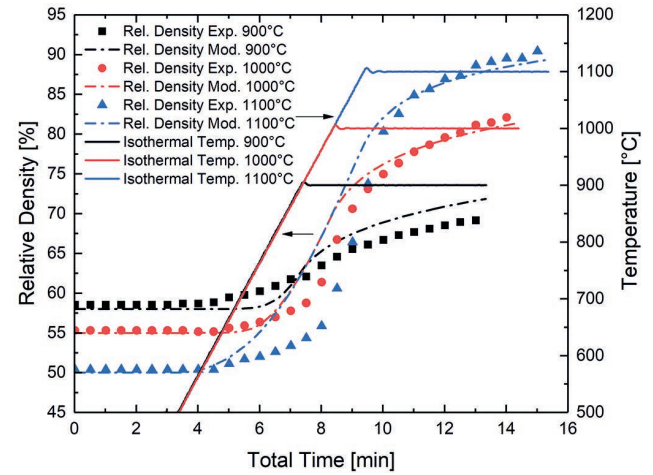


Fig. 11: Densification kinetics during FAST/SPS of GDC10 at 900 °C and 1100 °C with a dwell time of 6 minutes and pressure of 50 MPa.

Since densification is generally accompanied by the coarsening of grains, the influence of grain growth on the densification curves is considered in Fig. 13. For the analysis of the influence of grain growth on densification, the experiment with isothermal sintering at 1100 °C was selected. The temperature profile and the experimental evolution of the relative density are plotted in Fig. 13 as a solid curve and solid square symbol, respectively. Two densification curves were modeled, one considering the densification with grain growth (represented by the black dash curve) and the other without grain growth (represented by red dash-dot curve). Grain growth during sintering hinders the densification process. This can also be evidently seen in the plot where the model considering the grain growth fits better to the experimental values in comparison with the model without grain growth.

Table 1: Model parameters for GDC10

Parameter	Description	Value	Source
$B \cdot \Phi_0$	Constant · pre-exponential term	$8.59 \cdot 10^{11} \text{ m}^2/\text{s}$	Fit
σ_{ex}	Applied macroscopic stress	50 MPa	Experiment
E_{th}	Young's modulus	165 GPa	[3]
ν_{eff}	Poisson's ratio	0.3	[3]
b	Burgers vector	$3.96 \cdot 10^{-10} \text{ m}$	[14]
K_0	Pre-exponential constant	$2.0 \cdot 10^{-9} \text{ m}^2/\text{s}$	Fit

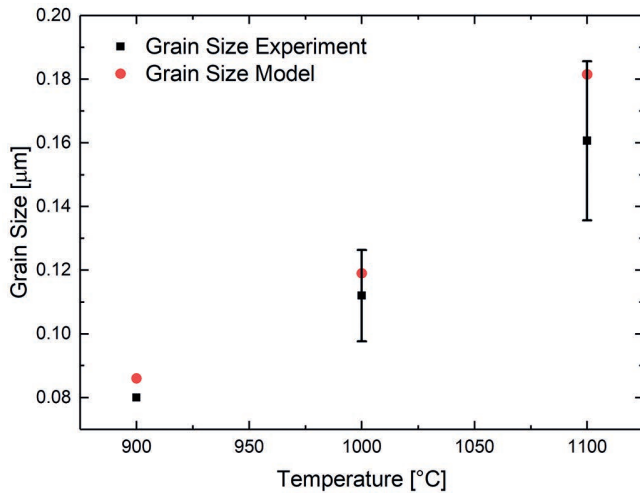


Fig. 12: Grain growth kinetics during FAST/SPS of GDC10 at 1100 °C with different dwell times and pressure of 50 MPa.

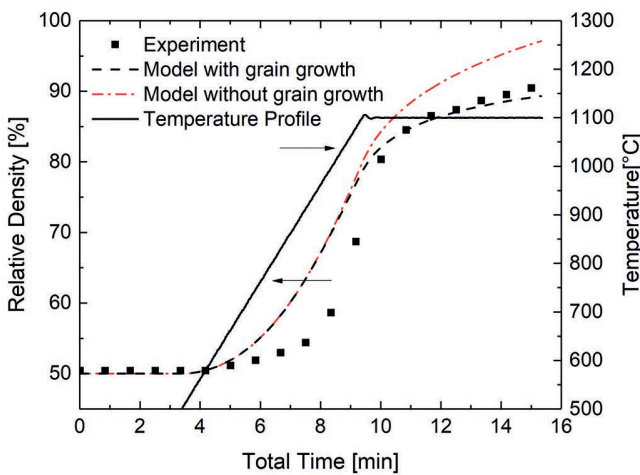


Fig. 13: Sintering model with and without grain growth for sintering temperature of 1100 °C and dwell time of 6 min.

V. Discussion

Owing to the self-diffusion of atoms that occurs in polycrystalline materials exposed to external loads at elevated temperatures, atoms diffuse from interfaces under compression and to grain boundaries under tension. Such a creep mechanism is commonly known as Nabarro-Herring creep. Creep also occurs when diffusion of matter occurs along the grain boundaries, that is termed Coble creep. Contrary to Nabarro Herring creep or Coble creep, activation of matter transport also occurs owing to dislocation movement arising from the application of high stresses. In such cases, n depends on the dislocation motion and has values between 3 and 10¹⁸.

For GDC10, Routbort¹⁹ *et al.* conducted compression creep tests on dense samples and reported a n value of 1.3 ± 0.2 and activation energy for creep deformation of 480 kJ/mol for temperature ranges of 1200–1300 °C and applied pressures of 10–100 MPa. The authors related the activation energy to the creep deformation process controlled by cerium-cation diffusion. Lipinska-Chwalek *et al.*^{20,21} reported stress exponent values, for different cerium oxide materials, between 0.5 and 2.5. In those cases,

compression creep tests were performed on dense samples at relatively low temperatures (800–900 °C) and applied pressures of 30–120 MPa. There, the activation energies calculated had values between 50–160 kJ/mol. The authors, thereby, suggested that the dominating creep deformation mechanism could be a combination of diffusion- and dislocation-based mechanisms.

Densification, in a sintering process, is generally accompanied by grain coarsening, where the grains increase in size and decrease in number. To achieve a more accurate prediction of the densification, the modeling procedure should integrate a grain growth law, as presented in this study. For GDC10, Ni *et al.*¹⁵ reported a similar grain growth exponent value, an activation energy for grain growth of 427 ± 22 kJ/mol and suggested that the grain growth predominantly proceeds through grain boundary diffusion. This suggests that the dominant mechanism for grain growth is grain boundary diffusion. The differences in the activation energies of the present study might be attributed to the presence of higher heating rates and the application of pressure.

He *et al.* studied free sintering of GDC10, under reducing conditions (H₂/N₂) and normal atmosphere²². The sintering kinetics were enhanced in the early stage of sintering owing to the formation of oxygen vacancies, under low oxygen partial pressure conditions. Densification activation energies of around 290 ± 20 kJ/mol under reducing conditions were reported. The activation energy for the densification of GDC10 calculated in this work is very close to the activation energy reported by He *et al.*²². In FAST/SPS experiments conducted under vacuum conditions with graphite tools, a localized reduced atmosphere is created around the green GDC10 sample. Owing to the reduction environment, there is a release of oxygen vacancies from GDC10 caused by the reduction of Ce⁴⁺ to Ce³⁺.

With the comparison of the stress exponent and the activation energy for densification and grain growth measured in this work with the literature values discussed above, the expected dominating deformation/densification mechanism is a combination of diffusion- and dislocation-based mechanism.

In solid-state sintering, the stages of sintering represent the geometrical transition of a powder compact to a strong object²³. In the initial stage, particles rearrange themselves to allow contact between particles to grow. In the intermediate stage, the necks formed grow to leave a tubular network between pores, and in the final stage the tubular pores vanish to form spherical ones. In this work, from the densification curves plotted in Fig. 11, the curves could be divided into the afore-mentioned regions. We observe that for all the temperatures before the isothermal stages start a significant amount of densification occurs. Particle rearrangement could contribute to the initial densification in the early stages. It is believed that by considering a phenomenological approach for the contribution for particle rearrangement during the early stages of sintering, as mentioned in Kraft *et al.*²⁴, the model could be improved. Implementing the densification model in finite element (FE) simulations^{24–26} would also provide a better understanding of the densification process as the initial density distri-

butions, temperature distributions during FAST and grain size distributions can be considered for the analysis.

VI. Conclusions

This work investigated the densification and grain growth kinetics during FAST/SPS of GDC10. The sintering kinetics and activation energy of densification have been determined using isothermal sintering at various temperatures with constant uniaxial pressure. The results indicate that in a low sintering temperature regime (900–1100 °C), the average stress exponent and the activation energy are 2 and 260 kJ/mol, respectively. Similarly, the grain growth kinetics and activation energy of grain growth have also been determined by analyzing the evolution of grain sizes under isothermal sintering conditions. This led to utilizing a grain growth exponent of 2 and activation energy for grain growth of around 200 kJ/mol. Both densification and sintering kinetics indicate the dominating densification mechanism to be a combination of diffusion- and dislocation-based mechanism. However, at higher temperatures, the densification could be dominated purely by the dislocation-based mechanism. A numerical densification model has been utilized in the current study and it can be used to predict the FAST/SPS densification and grain growth curves of the sintering of GDC10. Furthermore, the accuracy is increased when the model is integrated with a grain growth law.

Acknowledgments

Funding by the Deutsche Forschungsgemeinschaft (DFG, German Research Foundation) – Priority Programme (SPP) 1959/1 [BR 1844/21-1] is gratefully acknowledged.

References

- Guillon, O., Gonzalez-Julian, J., Dargatz, B., Kessel, T., Schierning, G., *et al.*: Field-assisted sintering technology/spark plasma sintering: Mechanisms, materials, and technology developments, *Adv. Eng. Mater.*, **16**, 830–849, (2014), DOI: 10.1002/adem.201300409.
- Munir, Z.A., Anselmi-Tamburini, U., Ohyanagi, M.: The effect of electric field and pressure on the synthesis and consolidation of materials: A review of the spark plasma sintering method, *J. Mater. Sci.*, **41**, 763–77, (2006), DOI: 10.1007/s10853-006-6555-2.
- Mogensen, M., Sammes, N.M., Tompsett, G.A.: Physical, chemical and electrochemical properties of pure and doped ceria, *Solid State Ionics*, **129**, 63–94, (2000), DOI: 10.1016/S0167-2738(99)00318-5.
- Brandon, N.P., Corcoran, D., Cummins, D., Duckett, A., El-Khoury, K., *et al.*: Development of metal supported solid oxide fuel cells for operation at 500–600 °C, *J. Mater. Eng. Perform.*, **13**, 253–256, (2004), DOI: 10.1361/10599490419135.
- Rojek, V., Roehrens, D., Brandner, M., Menzler, N.H., Guillon, O., *et al.*: Development of high performance anodes for metal-supported fuel cells, *ECS Trans.*, **68**, 1297–1307, (2015), DOI: 10.1149/06801.1297ecst.
- Nielsen, J., Sudireddy, B.R., Hagen, A., Persson, Å.H.: Performance factors and sulfur tolerance of metal supported solid oxide fuel cells with nanostructured Ni:GDC infiltrated anodes, *J. Electrochem. Soc.*, **163**, F574–F580, (2016), DOI: 10.1149/2.1081606jes.
- Bernard-Granger, G., Guizard, C.: Spark plasma sintering of a commercially available granulated zirconia powder: I. sintering path and hypotheses about the mechanism(s) controlling densification, *Acta Metall.*, **55**, 3493–3504, (2007), DOI: 10.1016/j.actamat.2007.01.048.
- Bernard-Granger, G., Addad, A., Fantozzi, G., Bonnefont, G., Guizard, C., *et al.*: Spark plasma sintering of a commercially available granulated zirconia powder: Comparison with hot-pressing, *Acta Metall.*, **58**, 3390–3399, (2010), DOI: 10.1016/j.actamat.2010.02.013.
- Langer, J., Hoffmann, M.J., Guillon, O.: Direct comparison between hot pressing and electric field-assisted sintering of submicron alumina, *Acta Metall.*, **57**, 5454–5465, (2009), DOI: 10.1016/j.actamat.2009.07.043.
- Langer, J., Hoffmann, M.J., Guillon, O.: Electric field-assisted sintering and hot pressing of semiconductive zinc Oxide: A comparative study, *J. Am. Ceram. Soc.*, **94**, 2344–2353, (2011), DOI: 10.1111/j.1551-2916.2011.04396.x.
- Langer, J., Hoffmann, M.J., Guillon, O.: Electric field-assisted sintering in comparison with the hot pressing of yttria-stabilized zirconia, *J. Am. Ceram. Soc.*, **94**, 24–31, (2011), DOI: 10.1111/j.1551-2916.2010.04016.x.
- Chakravarty, D., Chokshi, A.H.: Direct characterizing of densification mechanisms during spark plasma sintering, *J. Am. Ceram. Soc.*, **97**, 765–771, (2014), DOI: 10.1111/jace.12796.
- Trzaska, Z., Cours, R., Monchoux, J.-P.: Densification of Ni and TiAl by SPS: kinetics and microscopic mechanisms, *Metall. Mater. Trans. A*, **49**, 4849–4859, (2018), DOI: 10.1007/s11661-018-4775-0.
- Guyot, P., Antou, G., Pradeilles, N., Weibel, A., Vandenhenne, M., *et al.*: Hot pressing and spark plasma sintering of alumina: discussion about an analytical modelling used for sintering mechanism determination, *Scripta Mater.*, **84–85**, 35–38, (2014), DOI: 10.1016/j.scriptamat.2014.04.013.
- Ni, D.W., Schmidt, C.G., Teocoli, F., Kaiser, A., Andersen, K.B., *et al.*: Densification and grain growth during sintering of porous $\text{Ce}_{0.9}\text{Gd}_{0.1}\text{O}_{1.95}$ tape cast layers: A comprehensive study on heuristic methods, *J. Eur. Ceram. Soc.*, **33**, 2529–2537, (2013), DOI: 10.1016/j.jeurceramsoc.2013.03.025.
- Chen, I.-W.: Grain boundary kinetics in oxide ceramics with the cubic fluorite crystal structure and its derivatives, *Interface Sci.*, **8**, 147–156, (2000), DOI: 10.1023/A:1008742404071.
- Frost, H.J., Ashby, M.F.: Deformation-mechanism maps: The plasticity and creep of metals and ceramics. Oxford, Paris: Pergamon Press; 1982.
- Rahaman, M.N.: Sintering of ceramics. Boca Ratón, Florida: CRC Press; 2008.
- Routbort, J.L., Goretta, K.C., Arellano-López, A.R. de, Wolfenstine, J.: Creep of $\text{Ce}_{0.9}\text{Gd}_{0.1}\text{O}_{1.95}$, *Scripta Mater.*, **38**, 315–320, (1997), DOI: 10.1016/S1359-6462(97)00452-1.
- Lipińska-Chwałek, M., Pećanac, G., Malzbender, J.: Creep behaviour of membrane and substrate materials for oxygen separation units, *J. Eur. Ceram. Soc.*, **33**, 1841–1848, (2013), DOI: 10.1016/j.jeurceramsoc.2013.02.007.
- Lipińska-Chwałek, M., Schulze-Küppers, F., Malzbender, J.: Mechanical properties of pure and doped cerium oxide, *J. Eur. Ceram. Soc.*, **35**, 1539–1547, (2015), DOI: 10.1016/j.jeurceramsoc.2014.11.036.
- He, Z., Yuan, H., Glasscock, J.A., Chatzichristodoulou, C., Phair, J.W., *et al.*: Densification and grain growth during early-stage sintering of $\text{Ce}_{0.9}\text{Gd}_{0.1}\text{O}_{1.95-\delta}$ in a reducing atmosphere, *Acta Metall.*, **58**, 3860–3866, (2010), DOI: 10.1016/j.actamat.2010.03.046.
- German, R.M.: Geometric trajectories during sintering. In: Sintering: From empirical observations to scientific principles: Elsevier; 141–181, (2014), DOI: 10.1016/B978-0-12-401682-8.00006-9.

- ²⁴ Kraft, T., Riedel, H.: Numerical simulation of solid state sintering; model and application, *J. Eur. Ceram. Soc.*, **24**, 345–61, (2004), DOI: 10.1016/S0955–2219(03)00222-X.
- ²⁵ Reiterer, M., Kraft, T., Riedel, H.: Manufacturing of a gear wheel made from reaction bonded alumina—numerical simulation of the sinterforming process, *J. Eur. Ceram. Soc.*, **24**, 239–246, (2004), DOI: 10.1016/S0955–2219(03)00240–1.
- ²⁶ van Nguyen, C., Sistla, S.K., van Kempen, S., Giang, N.A., Bezold, A., *et al.*: A comparative study of different sintering models for Al_2O_3 , *J. Ceram. Soc. Japan*, **124**, 301–312, (2016), DOI: 10.2109/jcersj2.15257.

